ORIGINAL ARTICLE

Harnessing Natural Killer Immunity in Metastatic SCLC

Sarah A. Best, PhD,[a,b] Jonas B. Hess, MSc,[a,b] Fernando Souza-Fonseca-Guimaraes, PhD,[c,d,e] Joseph Cursons, PhD,[b,f,g] Ariena Kersbergen, BASc,[a] Xueyi Dong, BSc (Hons),[b,h] Jai Rautela, PhD,[g] Stephanie R. Hyslop, BSc (Hons),[a,b] Matthew E. Ritchie, PhD,[h,i] Melissa J. Davis, PhD,[b,f] Tracy L. Leong, MD, PhD,[j,k,l] Louis Irving, MD, PhD,[j,m] Daniel Steinfort, MD, PhD,[j,m] Nicholas D. Huntington, PhD,[b,e,g] Kate D. Sutherland, PhD[a,b,*]

[a]*ACRF Cancer Biology and Stem Cells Division, The Walter and Eliza Hall Institute of Medical Research, Parkville, Victoria, Australia*
[b]*Department of Medical Biology, The University of Melbourne, Parkville, Victoria, Australia*
[c]*University of Queensland Diamantina Institute, University of Queensland, Brisbane, Queensland, Australia*
[d]*Translational Research Institute, Brisbane, Queensland, Australia*
[e]*Molecular Immunology Division, The Walter and Eliza Hall Institute of Medical Research, Parkville, Victoria, Australia*
[f]*Bioinformatics Division, The Walter and Eliza Hall Institute of Medical Research, Parkville, Victoria, Australia*
[g]*Department of Biochemistry and Molecular Biology, Biomedicine Discovery Institute, Monash University, Clayton, Victoria, Australia*
[h]*Epigenetics and Development Division, The Walter and Eliza Hall Institute of Medical Research, Parkville, Victoria, Australia*
[i]*School of Mathematics and Statistics, The University of Melbourne, Parkville, Australia*
[j]*Department of Medicine, University of Melbourne, Parkville, Victoria, Australia*
[k]*Department of Respiratory and Sleep Medicine, Austin Hospital, Heidelberg, Victoria, Australia*
[l]*Personalised Oncology Division, The Walter and Eliza Hall Institute of Medical Research, Parkville, Victoria, Australia*
[m]*Department of Respiratory Medicine, Royal Melbourne Hospital, Parkville, Victoria, Australia*

Received 5 December 2019; revised 31 March 2020; accepted 7 May 2020
Available online - 26 May 2020

ABSTRACT

Introduction: SCLC is the most aggressive subtype of lung cancer, and though most patients initially respond to platinum-based chemotherapy, resistance develops rapidly. Immunotherapy holds promise in the treatment of lung cancer; however, patients with SCLC exhibit poor overall responses highlighting the necessity for alternative approaches. Natural killer (NK) cells are an alternative to T cell-based immunotherapies that do not require sensitization to antigens presented on the surface of tumor cells.

Methods: We investigated the immunophenotype of human SCLC tumors by both flow cytometry on fresh samples and bioinformatic analysis. Cell lines generated from murine SCLC were transplanted into mice lacking key cytotoxic immune cells. Subcutaneous tumor growth, metastatic dissemination, and activation of $CD8^+$ T and NK cells were evaluated by histology and flow cytometry.

Results: Transcriptomic analysis of human SCLC tumors revealed heterogeneous immune checkpoint and cytotoxic signature profiles. Using sophisticated, genetically engineered mouse models, we reported that the absence of NK cells, but not $CD8^+$ T cells, substantially enhanced metastatic dissemination of SCLC tumor cells in vivo. Moreover, hyperactivation of NK cell activity through augmentation of interleukin-15 or transforming growth factor-β signaling pathways ameliorated SCLC metastases, an effect that was

*Corresponding author.

Dr. Best and Mr. Hess contributed equally to this work.

Disclosure: Drs. Huntington and Rautela are cofounders and Drs. Cursons, Rautela, and Huntington are shareholders of oNKo-Innate Pty Ltd.

Address for correspondence: Kate D. Sutherland, PhD, ACRF Cancer Biology and Stem Cells Division, The Walter and Eliza Hall Institute of Medical Research, 1G Royal Parade, Parkville, Victoria 3052, Australia. E-mail: sutherland.k@wehi.edu.au

© 2020 International Association for the Study of Lung Cancer. Published by Elsevier Inc. This is an open access article under the CC BY-NC-ND license (http://creativecommons.org/licenses/by-nc-nd/4.0/).

ISSN: 1556-0864
https://doi.org/10.1016/j.jtho.2020.05.008

enhanced when combined with antiprogrammed cell death-1 therapy.

Conclusions: These proof-of-principle findings provide a rationale for exploiting the antitumor functions of NK cells in the treatment of patients with SCLC. Moreover, the distinct immune profiles of SCLC subtypes reveal an unappreciated level of heterogeneity that warrants further investigation in the stratification of patients for immunotherapy.

Keywords: SCLC; Small cell lung cancer; Metastasis; NK; Natural killer cells; GEMMs; Genetically engineered mouse models; PD-1; Programmed cell death-protein 1

Introduction

SCLC is a highly malignant neuroendocrine tumor that represents approximately 13% of lung cancer diagnoses annually in the United States.[1] The ability of SCLC tumor cells to disseminate early and establish metastases is a major cause of death.[2] It has recently been appreciated that SCLC is a heterogenous disease, in which four key transcriptional regulators define the emerging subtypes of SCLC, likely effecting clinical outcomes.[3] Although most patients with SCLC initially respond to platinum-based chemotherapeutic agents, resistance develops rapidly in 95% of patients resulting in an overall 5-year survival rate of less than 7%.[4] Coupled with a lack of major treatment advances for patients with SCLC in more than 30 years,[5] in 2012, the National Cancer Institute declared SCLC a recalcitrant cancer. Together, this highlights the urgent need for new therapeutic approaches that target primary and metastatic disease.

Immune checkpoint blockade (ICB), such as monoclonal antibodies targeting T cell checkpoint (programmed cell death-protein 1 [PD-1], programmed death-ligand 1 [PD-L1]) and inhibition (CTLA-4) pathways, unleash the T cell response to eliminate tumor cells. T cells identify tumor cells with human leukocyte antigen (HLA) presenting altered or unique peptides. Therefore, tumors with a high mutational burden are thought to be predictive of response to ICB.[6,7] Nevertheless, despite having one of the highest mutational burdens,[8] patients with SCLC exhibit a remarkably poor overall response rate to ICB, likely owing to low HLA expression.[9] Atezolizumab (anti–PD-L1) in combination with first-line chemotherapy (carboplatin and etoposide) in extensive-stage SCLC has recently been approved by the Food and Drug Administration (IMpower133); however, it provides a mere 2-month survival benefit to patients.[10] Although encouraging and providing evidence of immune surveillance, most patients with SCLC fail to respond to conventional T cell-based immunotherapies.

In addition to identifying approaches to enhance penetrance, durability, and response rates of ICB, there is an intense emerging interest in targeting additional cytotoxic effector populations, including natural killer (NK) cells.[11] NK cells are an attractive alternative target in cancer immunotherapy as they preferentially target altered or stressed ligands often up-regulated on tumor cells without dependency on neo-antigen and HLA expression. Notably, in murine models, NK cells are effective at resisting pervasive spread of experimental and spontaneous tumor metastases.[12] Indeed, NK cells can eliminate melanoma and breast cancer cells directly, and this activity is governed to a large extent by inflammatory cytokines, such as interleukin (IL)-15, and inhibitory signals, such as members of the transforming growth factor (TGF)-β superfamily.[12-15] Clinically, NK activity has been inversely correlated with cancer incidence, and NK cell infiltration in human tumors is associated with better prognosis in NSCLC, melanoma, gastric, and colorectal carcinomas.[16,17]

Here, we profiled the immune microenvironment of human and murine SCLC by interrogating gene expression signatures. Furthermore, by harnessing the power of in vivo genetic model systems, we have systematically evaluated the function of critical cytotoxic immune cell populations responsible for controlling SCLC progression. Together, these studies highlight adjunct approaches to redirect the immune system in the treatment of SCLC.

Materials and Methods

Patient Samples

We received all patient materials according to protocols approved by the Human Research Ethics Committee of the Walter and Eliza Hall Institute of Medical Research (approval #10/04). SCLC samples were obtained by endobronchial ultrasound-guided transbronchial needle aspirate (EBUS-TBNA), in which the Victorian Cancer Bank deidentified and consented patients to participate in this study. EBUS-TBNA biopsy and blood samples (ethylenediaminetetraacetic acid [EDTA] K2E collection tubes) were maintained at 4°C before processing.

Mice

All animal experiments were conducted in accordance with the regulatory standards approved by the Animal Ethics Committee of the Walter and Eliza Hall

Institute of Medical Research (AEC 2016.024). *Rb1*$^{fl/fl}$/*p53*$^{fl/fl}$,[18] *Mcl1*$^{NKp46\Delta/\Delta}$,[14] *Cish*$^{-/-}$,[12] *TGFβRII*$^{NKp46\Delta/\Delta}$,[19] *Prf1*$^{-/-}$,[20] and *IFN-γ*$^{-/-}$[21] mice have been previously described. All mice were maintained on a pure C67BL/6 background. For spontaneous SCLC development, 6- to 8-week-old *Rb1*$^{fl/fl}$/*p53*$^{fl/fl}$ mice were intranasally administered 20 μL 1 × 10^{10} pfu/mL Ad5-CMV-Cre (University of Iowa Gene Transfer Core Facility) as described previously.[22]

Cell Culture and Transplantation

The RP-nontransduced (RP-NT) cell line was established from a female C57BL/6 *Rb1*$^{\Delta/\Delta}$/*p53*$^{\Delta/\Delta}$ spontaneous primary lung SCLC lesion and maintained in culture as spheroids in 10% fetal bovine serum (FBS) (Sigma-Aldrich), 100 U/mL penicillin (Gibco), 100 μg/mL streptomycin (Gibco), 0.04 mg/mL hydrocortisone (Sigma-Aldrich), 1× Insulin-Transferrin-Selenium-Ethanolamine (Gibco), and 5 ng/mL murine epidermal growth factor (Thermo Fisher) in DMEM-F12 plus GlutaMAX (Gibco). The reporter RP-transduced (RP-T) cells were generated by transduction of pMSCV-Luc2-IRES-mCherry retroviral vector[23] by spin infection on six-well plates coated with 100 μg/mL retronectin (Takara Bio) and blocked in 2% bovine serum albumin (Sigma-Aldrich). The RP-T cells were then expanded and selected by flow cytometry based on mCherry expression. For subcutaneous (SQ) route, 1 × 10^6 RP-NT cells were resuspended in 50% growth factor–reduced Matrigel (Thermo #356231) and injected at a final volume of 100 μL. The tumors were caliper-measured three times per week, and volume was calculated using the following formula: (width × height^2) / 2. For intravenous injection (IV), 5 × 10^5 RP-NT or RP-T cells were resuspended in 200 μL phosphate buffered saline (PBS) and injected into the tail vein. Mice were collected at a single time point or aged for survival analysis. Bioluminescence signal was measured using the IVIS Spectrum (Perkin Elmer) within 15 minutes of a 3 mg intraperitoneal (IP) injection of luciferin (Thermo 122799).

Immune Cell Treatment

CD8$^+$ T cells were depleted using 100 μg anti-CD8 antibody (53.5.8 BioXCell BE0223) or isotype (2A3 BioXCell BE0089) injected 3 days before, on the day of, and weekly after RP cell injection. For ICB treatment, 200 μg anti–PD-1 (RMP 1-14 BioXCell BE0146) or isotype was administered IP on days 0, 3, and 6 after RP cell injection and repeated in 20-day cycles. For activation of IL-15 receptor complex, super IL-2 (sIL-2) was generated by incubating 150 μg/mL S4B6 antibody (BioXCell BE0043) with 15 μg/mL rmIL-2 (Miltenyi Biotech 130-096-707) at 37°C for 30 minutes, and then, 150 μL was injected IP per mouse once weekly from 3 days after IV injection of the RP cells. Vehicle control mice received 150 μL PBS IP.

Flow Cytometry

The EBUS-TBNA samples were digested in 20 mg/mL collagenase I (Worthington LS004200) in 0.2 g/liter glucose (Sigma-Aldrich 50-99-7) supplemented with 0.03 mg/mL DNase (Worthington LS002140) at 160 rpm for 45 minutes at 37°C. After filtering through a 100 μm-mesh sieve, the sample was resuspended in 0.1 mg/mL DNase/155 mM NH_4Cl, 10 mM $KHCO_3$, and 1 mM Na_2EDTA for 3 minutes at 4°C. Peripheral blood mononuclear cells (PBMCs) were isolated using Ficoll (GE Healthcare 17-1440-03) gradient in 50 mL Leucosep tubes (Greiner Bio-One 227 290). The PBMCs were washed twice in 2% FBS/PBS and stored on ice. Mouse peripheral blood was obtained by mandible bleed into EDTA tubes (Sarstedt #20.1341.102). Red blood cells were lysed in 156 mM NH_4Cl/11.9 mM $NaHCO_3$/0.097 mM EDTA at a 100:1 ratio. The cells were washed in 2% FBS/PBS and resuspended in 200 μL 2% FBS/PBS before antibody staining. Tumor-bearing livers were dissociated in 20 mg/mL collagenase I with 0.2 g/liter glucose supplemented with 0.03 mg/mL DNase at 160 rpm for 45 minutes at 37°C and passed through 18G and 21G needles. Red blood cells were lysed in 0.8% NH_4Cl and resuspended in 200 μL 2% FBS/PBS before antibody staining. For flow cytometry, the cell pellets were resuspended at 1 × 10^6 per 40 μL in 2% FBS/PBS and blocked in 1:40 FcR and 1:80 Rat IgG for 30 minutes on ice as described previously[24] and stained with primary antibodies (Supplementary Table 1). After washing, the cells were resuspended in 0.1 mg/mL propidium iodide (Sigma-Aldrich 25535-16-4). Immune flow cytometry definitions are as follows: CD8$^+$ T cells (human: CD45$^+$CD3$^+$CD8$^+$; mouse: CD45$^+$CD3$^+$CD8$^+$); NK cells (human: CD45$^+$CD3$^-$CD56$^+$NKp46$^+$; mouse: CD45$^+$CD3$^-$DX5$^+$NKp46$^+$); tumor cells (human: CD45$^-$CD31$^-$CD140b$^-$CD235a$^-$EpCAM$^+$CD56$^+$; mouse: CD45$^-$CD31$^-$EpCAM$^+$NCAM$^+$), and DC1 dendritic cells (CD45$^+$CD11b$^-$CD103$^+$). For Granzyme B, IFN-γ, and Ki67, intracellular stains were performed using the eBioscience Transcription Factor Staining Buffer Set (Thermo Scientific 00-5523-00). Flow cytometry was performed using the ARIA III (BD Biosciences), and data were analyzed using FlowJo software version 10 (FlowJo LLC).

Immunohistochemistry

Tissues were fixed for 24 hours in 4% paraformaldehyde, and paraffin blocks were sectioned at 4 μm for immunohistochemistry or 2 μm for hematoxylin

Table 1. Patient With SCLC and EBUS Characteristics

Patient Information						Clinical Sample				
ID	Age, y	Sex	Smoking Status	Stage	EBUS Location[a]	Cytology	SYP	CD56	CgA	TTF1
17MH0072	67	M	Current	NA	Subcarina LN	SCLC	−	+	NA	+
17MH0091	57	F	Current	IV	Subcarina	SCLC	+	+	+	+
18MH0130	65	F	Former	Recurrent	Mediastinal LN 8	SCLC	+	+	−	+
18MH0157	65	M	Current	NA	7	SCLC	+	+	−	+
18MH0166	63	F	Current	NA	4LN	SCLC	NA	NA	NA	NA
18MH0170a	64	F	NA	Recurrent	4RLN	SCLC	+	+	−	+
18MH0170b					12RLN					

[a]LN stations are indicated according to the classification of Mountain and Dressler.43
EBUS, endobronchial ultrasound; F, female; LN, lymph node; M, male; NA; not available; RLN, recurrent laryngeal nerve.

and eosin stain. Antigen retrieval was performed on dewaxed slides followed by 3% hydrogen peroxide (Thermo FSBBP2633-500) in methanol. Ascl1 and NeuroD1 were probed in 10% milk with 0.5% PBS-Tween20, and Granzyme B was probed using the Mouse on Mouse Detection Kit (Vector Laboratories BMK-2202), with incubation in primary antibody (Supplementary Table 1) at 4°C overnight. Biotinylated secondary antibodies, Vectastain Elite ABC horseradish peroxidase reagent (Vector Laboratories PK-7100), and ImmPACT 3,3-diaminobenzidine peroxidase substrate (Vector Laboratories SK-4105) were performed according to standard procedures. The slides were counterstained in hematoxylin and coverslipped. Liver tumor burden was quantified on hematoxylin and eosin slides using the measure tool on ImageJ software (Softonic), and GranzymeB quantification was performed by manually counting the positive cells in four ×40 magnification images per liver section.

Quantitative Reverse Transcriptase Polymerase Chain Reaction

RNA was extracted from snap-frozen tumor tissue or cell pellets using the RNeasy mini kit (Qiagen #74104) and then converted to cDNA using the SuperScript III kit (Thermo 18080044). Quantitative reverse transcriptase polymerase chain reaction was performed on cDNA in 20 μL reactions using SyberGreen (Bioline QT615-05) with 10 μM primers (Supplementary Table 2) and run on the ViiA 7 real-time polymerase chain reaction system (Thermo Scientific) using standard conditions. The $\Delta\Delta$CT statistical method was used to calculate abundance of transcript relative to housekeeper control.

Software

Computational analyses were performed using Python (v 3.66) with the matplotlib,[25] numpy,[26] pandas,[27] scikit-learn,[28] and scipy[29] packages. The script used for data processing (described subsequently) and figure generation is available from https://github.com/DavisLaboratory/SCLC-NK-scoring.

Data

Human SCLC Data. Processed fragments per kilobase of transcript per million mapped reads (FPKM) RNA-sequencing (RNA-seq)/transcriptomic data and clinical annotation data (including stage) were taken directly from George et al.,[30] to allow gene set scoring with singscore, and the established gene sets at the transcript level data were collapsed to gene-level data using the median value. Where available, patient classifications were taken directly from Rudin et al.[3] For remaining patient samples, classifications were obtained by defining thresholds ($\log_2|\text{FPKM}+1|$) for the marker transcription factors YAP1 (2.5) and POU2F3 (2.5). Remaining samples were classified as ASCL1 or NEUROD1 subtype dependent on the relative expression of these transcription factors (Supplementary Fig. 1*C*) with a required difference of at least 1; 5 samples remained unclassified and were not included in further analyses.

Genetically Engineered Mouse Model Data. Processed FPKM RNA-seq data for mouse models of SCLC from Mollaoglu et al.[31] and corresponding sample annotation data were obtained from Gene Expression Omnibus (accession number GSE89660). Further microarray data from Schaffer et al.[32] were obtained from Gene Expression Omnibus (accession number GSE18534) and processed using the affy R/Bioconductor package[33–35] to compute robust multi-array analysis[36] normalized expression measures. Probes were annotated using the mouse4302.db[37] annotation package and mapped to human homologs through the MGI Vertebrate Homology resource (http://www.informatics.jax.org/homology.shtml) available from Mouse Genome Database.[38] To

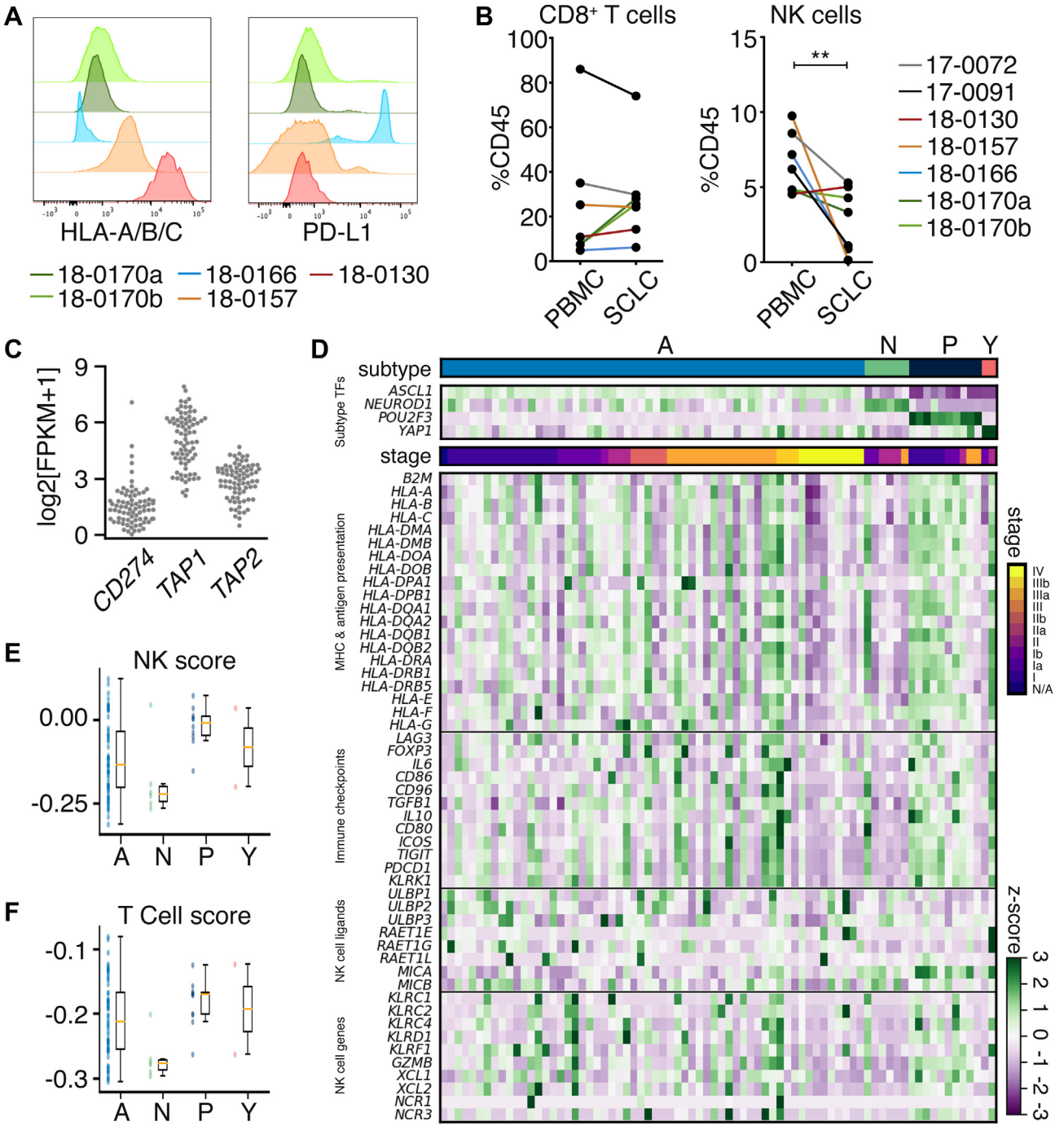

Figure 1. SCLC subsets have unique immune infiltration properties. (*A*) Flow cytometry quantification of HLA-A/B/C and PD-L1 cell surface expression on SCLC biopsies (n = 4 patients; Table 1). (*B*) Quantification of $CD8^+$ T cells and NK cells as a proportion of $CD45^+$ cells in PBMC and matched SCLC sample (n = 6 patients). Wilcoxon paired *t* test $^{**}p = 0.0062$. (*C*) RNA transcript abundance for *CD274*, *TAP1*, and *TAP2* from George et al.[30] (*D*) SCLC subtype, clinical stage, and z-score normalized RNA transcript abundance for annotated selections of genes. Subtypes: ASCL1 (A), NEUROD1 (N), POU2F3 (P), and YAP1 (Y). (*E*) NK cell and (*F*) T cell scores for bulk RNA-sequencing samples grouped by SCLC subtype. FPKM, fragments per kilobase of transcript per million mapped reads; HLA, human leukocyte antigen; MHC, major histocompatibility complex; NA, not available; NK, natural killer; PBMC, peripheral blood mononuclear cell; PD-L1, programmed death-ligand 1; TF, transcription factor.

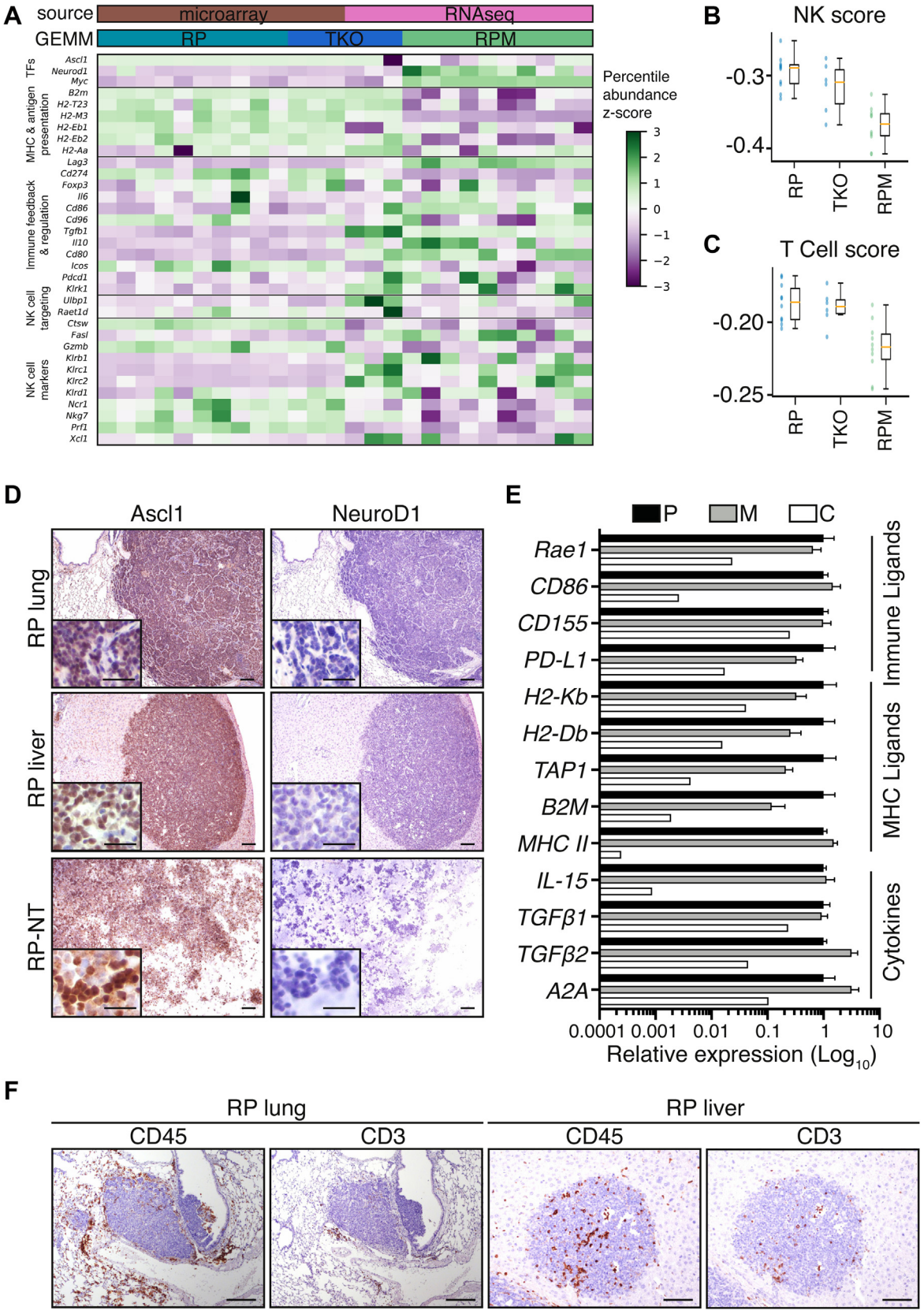

Figure 2. Mouse models of SCLC subsets display immune characteristics of human SCLC subsets. (*A*) SCLC mouse models and z-score percentile normalized transcript abundance data for annotated selections of genes. (*B*) NK cell and (*C*) T cell scores for bulk RNA-sequencing samples grouped by SCLC mouse model. (*D*) Immunostaining of NeuroD1 and Ascl1 on RP

make these data more comparable, genes were restricted to those present across both data sources and percentile normalized.

Gene Set Scoring. Gene set scoring was performed using the singscore method.[39] Briefly, the mean rank of a given gene set is calculated and normalized by the size of the gene set (and the corresponding theoretical minimum/maximum scores). Scores were generated using a NK cell gene set,[16] and a T cell gene set was obtained from the union of CIBERSORT/LM22[40] T cell gene signatures. For scoring of mouse data, set genes were converted to the closest known mouse-human paralog as defined by the Human Genome Organisation Gene Nomenclature Committee Comparison of Orthology Predictions.

Results

SCLC Subtypes Exhibit Unique Immune Microenvironments

To evaluate the immune infiltration of SCLC, we obtained EBUS-TBNA tumor material[41,42] and matched PBMCs from a cohort of patients with SCLC (Table 1).[43] Flow cytometric analysis of fresh samples identified a large variation in the expression of immune-active cell surface markers HLA-A/B/C and PD-L1 within the cohort (Fig. 1*A*). To better understand the functional effect of HLA and PD-L1 cell surface expression on the cytotoxic effector cells of the innate and adaptive immune systems, we quantified the proportion of $CD8^+$ T and NK cells within the SCLC sample relative to the circulating PBMCs in each patient. Although the differential expression of HLA-A/B/C and PD-L1 seemed to have less impact on $CD8^+$ T cell infiltration, NK cell tumor infiltration was significantly reduced in SCLC tumors relative to PBMCs across the patients (Fig. 1*B* and Supplementary Fig. 1*A*). The degree of reduction seemed to be concordant with the expression level of PD-L1, in which patients 18-0166 and 18-0157 had the highest expression of PD-L1 and the lowest infiltration of NK cells to the SCLC tumor, irrespective of the high levels of NK cells detected in the peripheral blood. To investigate these findings in a large cohort of patients, we used publicly available transcriptome data of 76 patients with stages I to IV SCLC.[30] Consistent with our patient cohort, transcriptome analysis identified a broad spectrum of expression of *CD274* (PD-L1), *TAP1*, *TAP2* (HLA components) (Fig. 1*C*) and transcripts of other immune activation factors (Supplementary Fig. 1*B*).

In the clinic, patients with SCLC achieve limited benefit from T cell-based checkpoint inhibition.[10] With the recent classification of SCLC into defined subtypes,[3] we hypothesized that immunogenicity is an inherent characteristic of each subtype. SCLC transcriptomic data[30] were stratified on the basis of the expression of *ASCL1*, *NEUROD1*, *POU2F3*, and *YAP1* (Supplementary Fig. 1*C*). Next, we investigated the immune regulatory capacity of each of the four subsets (Fig. 1*D*). Strikingly, the NEUROD1 subset exhibited the lowest expression of immune-related genes, whereas the POU2F3 subset consistently had the highest. Interestingly, the ASCL1 subset displayed a broad spectrum of immunogenicity, irrespective of patient stage (Fig. 1*D*). To interrogate the relationship of the SCLC subtypes on NK and $CD8^+$ T cells, we used a gene signature derived to predict infiltration in solid tumors.[16] Consistent with the transcriptional immune regulatory analysis, both NK (Fig. 1*E*) and T (Fig. 1*F*) cell scores were highest in the POU2F3 subset, suggesting this subtype of SCLC is the most immunogenic, whereas the ASCL1 subset displays a greater level of heterogeneity.

To model SCLC immune infiltration and activity, we used genetically engineered mouse models (GEMMs) generated reflecting the near-universal loss of *TP53* and *RB1* in SCLC.[30] We obtained sequencing data from the three most frequently used SCLC GEMMs, $Rb1^{\Delta/\Delta}/p53^{\Delta/\Delta}$ (RP),[18,44] RP/$p130^{\Delta/\Delta}$ (TKO),[32] and RP/Myc^{T58A} (RPM),[31] and stratified on the basis of expression of *Ascl1*, *NeuroD1*, and *Myc* (Fig. 2*A*). Consistent with previous studies, RPM was classified in the NeuroD1 subset,[31] whereas both RP and TKO mouse models displayed increased relative expression of both *Ascl1*. To date, no murine model exists that reflects the *Pou2f3* or *Yap1* SCLC subtype. Similar to the human immunoreactive ASCL1 subset, RP and TKO SCLC tumors expressed increased levels of major histocompatibility complex and antigen presentation genes relative to the $NeuroD1^+$ RPM model (Fig. 2*A*). Consistent with this broad analysis, application of the murine NK and T cell scores identified increased immune infiltration in RP and TKO tumors, with reduced scores in the $NeuroD1^+$ RPM subset (Fig. 2*B* and *C*). Therefore, the three often used SCLC mouse models largely represent the heterogeneity of patient samples.

($Rb1^{\Delta/\Delta}/p53^{\Delta/\Delta}$) spontaneous primary tumor (RP lung), RP-T liver metastasis (RP liver), and in vitro cell line (RP-NT). Scale, 100 μm; inset, 25 μm. (*E*) Quantitative RT-PCR of cytokine (*IL-15*, *TGFβ1*, *TGFβ2*, *A2A*), MHC ligand (*H2-Kb*, *H2-Db*, *TAP1*, *B2M*, *MHC-II*), and immune ligand (*Rae1a*, *CD86*, *CD155*, *PD-L1*) expression in cells isolated from RP primary tumor (n = 3), RP-T liver metastasis (n = 3), and RP-NT cell line (n = 1). Mean ± SEM. (*F*) Representative immunostaining of CD45 and CD3 on RP primary lung tumor and RP-T liver metastasis. Scale, 100 μm. GEMM, genetically engineered mouse model; MHC, major histocompatibility complex; NK, natural killer; RNA-Seq, RNA-sequencing; RP-NT, RP-nontransduced; RP-T, RP-transduced; RT-PCR, reverse transcriptase polymerase chain reaction; TF, transcription factor.

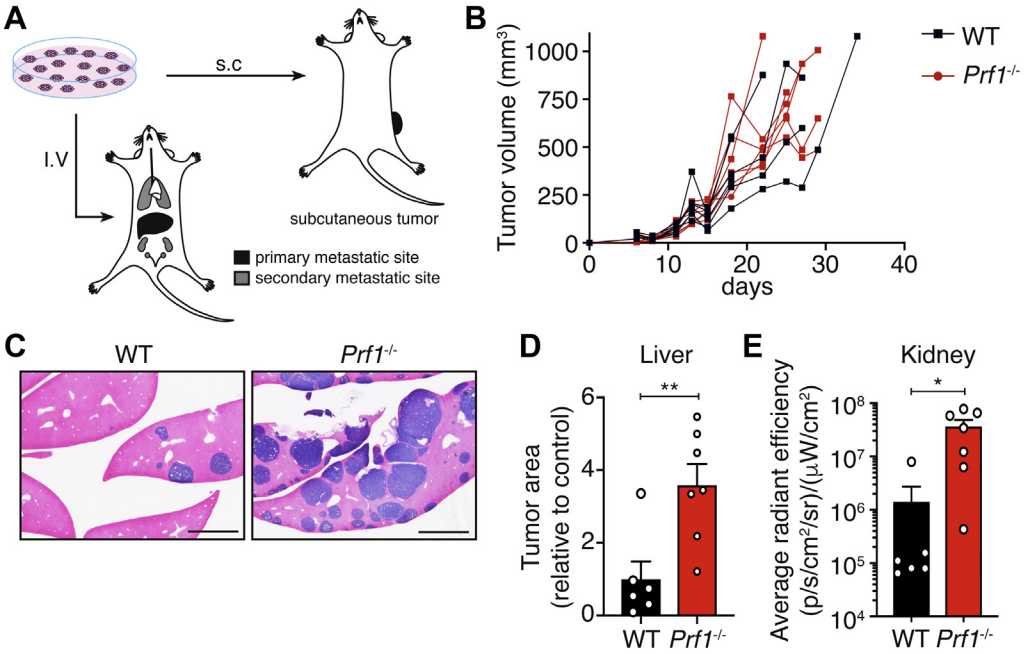

Figure 3. Cytotoxic immune cells control SCLC metastatic spread. (*A*) Schematic of tumor transplantation models. To monitor "primary" tumor growth, 1×10^6 RP cells were injected SQ into the flanks of C57BL/6 or immune-modified recipient mice. To monitor metastatic dissemination, 0.5×10^6 RP cells were injected IV into C57BL/6 or immune-modified recipient mice. Metastatic tumor burden (primary site: liver; secondary sites: ovary, kidney, lung) was evaluated by histology and imaging. (*B*) Primary growth model of RP-NT cells in WT (C57BL/6; n = 6) and *Prf1*$^{-/-}$ (n = 6) recipient mice. (*C*) H&E-stained livers 30 days after IV injection of RP-T cells into C57BL/6 (n = 6), and *Prf1*$^{-/-}$ (n = 7) recipient mice. Scale, 1 mm. (*D*) Quantification of tumor burden as percentage of liver area containing metastatic nodules. Mean ± SEM. Ordinary one-way ANOVA/Dunnett's multiple comparisons test $^{**}p = 0.0042$. (*E*) Quantification of mCherry signal in distant metastases to the kidney in C57BL/6 (n = 6) and *Prf1*$^{-/-}$ (n = 7) recipient mice. Mean ± SEM. Unpaired Student's *t* test $^{*}p = 0.0199$. H&E, hematoxylin and eosin; IV, intravenous; RP-NT, RP-nontransduced; RP-T, RP-transduced; SQ, subcutaneous; WT, wild type.

To model the progression of SCLC in the immunoreactive RP GEMM, we generated a primary mouse tumor cell line from an Ad5-CMV-Cre-infected RP SCLC lung nodule (RP-NT). RP-NT grows as nonadherent spheres in tissue culture, and when injected IV into syngeneic C57BL/6 mice, gives rise to metastatic tumor nodules primarily in the liver, consistent with previous investigations.[45] Critically, RP-NT represents the ASCL1$^+$ subtype, consistent with the high Ascl1 expression seen in primary and metastatic lesions in RP mice (Fig. 2*D*). Although the expression of immune ligands is downregulated in RP-NT in vitro, metastatic nodules derived from IV injection of RP-NT display similar expression patterns compared with spontaneous RP primary tumors dissected from the lung (Fig. 2*E* and Supplementary Fig. 2). In line with these findings, CD45$^+$ CD3$^+$ T cells seem to be excluded from SCLC lung tumors, whereas variegated infiltration was seen in liver SCLC nodules (Fig. 2*F*).

Cytotoxic Mediators Control SCLC Tumor Dissemination

To investigate cytotoxic immune cell control in the development and progression of SCLC, we performed transplantation studies in immune-modified recipient mice. We modeled primary tumor growth through SQ injection and metastatic dissemination to the liver through IV injection (Fig. 3*A*). To reveal the requirement of cytotoxic immune cell-mediated control, RP-NT were SQ transplanted into *Perforin*-knockout (*Prf1*$^{-/-}$)[20] recipient mice. Consistent with previous studies,[46] loss of activity in cytotoxic mediators did not alter SQ tumor growth (Fig. 3*B*). Next, to monitor metastatic dissemination, we engineered the RP-NT cell line to express an mCherry-luciferase reporter construct (RP-T). Strikingly, loss of perforin-mediated immune cell killing unleashed the metastatic potential of the SCLC RP-T cells, with a significant increase in liver metastatic nodules (Fig. 3*C* and *D*) and tumor burden in secondary sites (Fig. 3*E*) observed 30 days after IV injection. To confirm the magnitude of response to loss of cytotoxic-mediated cell death, we modeled metastasis in IFN-γ knockout mice (*IFN-γ*$^{-/-}$),[21] which lack the key effector molecule of both NK and CD8$^+$ T cells. Consistent with deficiency in perforin-mediated cell killing, *IFN-γ*$^{-/-}$ recipient mice displayed significantly increased tumor burden in the liver and secondary metastatic sites (Supplementary Fig. 3). Taken together, we find that cytotoxic immune cells are crucial for the control of SCLC metastasis.

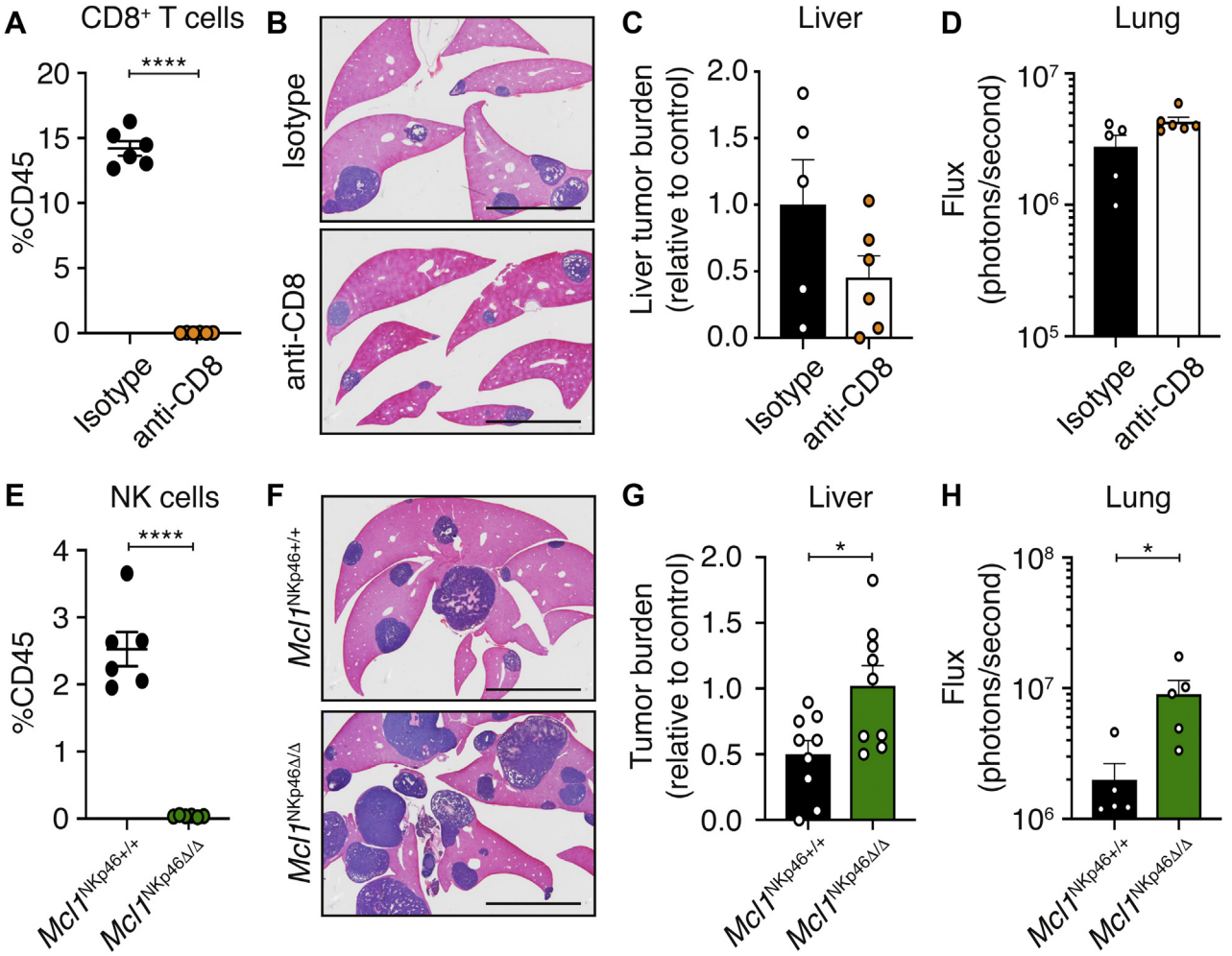

Figure 4. NK cells control the metastatic spread of SCLC. (*A*) Quantification of $CD8^+$ T cells in the peripheral blood of C57BL/6 mice treated with isotype (n = 6) or anti-CD8 (n = 6) antibody. Mean ± SEM. Unpaired student's *t* test ****$p < 0.0001$. (*B*) Representative H&E-stained livers 30 days after IV injection of RP-T cells into C57BL/6 mice treated with isotype or anti-CD8 antibody. Scale, 5 mm. (*C*) Quantification of liver tumor burden of C57BL/6 mice treated with isotype (n = 6) or anti-CD8 (n = 6) antibody. Mean ± SEM. (*D*) Quantification of luciferase signal in the lungs of C57BL/6 mice treated with isotype (n = 6) or anti-CD8 (n = 6) antibody. Mean ± SEM. (*E*) Quantification of NK cells in the peripheral blood of $Mcl1^{NKp46+/+}$ (n = 6) and $Mcl1^{NKp46\Delta/\Delta}$ (n = 6) mice. Mean ± SEM. Unpaired student's *t* test ****$p < 0.0001$. (*F*) Representative H&E-stained livers 30 days after IV injection of RP-T cells into $Mcl1^{NKp46\Delta/\Delta}$ and $Mcl1^{NKp46+/+}$ controls. Scale, 5 mm. (*G*) Quantification of tumor burden in $Mcl1^{NKp46+/+}$ (n = 6) and $Mcl1^{NKp46\Delta/\Delta}$ (n = 6) mice. Mean ± SEM. (*H*) Quantification of luciferase signal in the lungs of $Mcl1^{NKp46+/+}$ (n = 6) and $Mcl1^{NKp46\Delta/\Delta}$ (n = 6) recipient mice. H&E, hematoxylin and eosin; IV, intravenous; NK, natural killer; RP-T, RP-transduced.

NK Cells Control SCLC Dissemination

To investigate which cytotoxic immune cells are critical for immunosurveillance of SCLC, we interrogated the action of $CD8^+$ T cells and NK cells in the metastatic setting. Depletion of $CD8^+$ T cells was achieved using an anti–CD8 antibody, which efficiently depleted $CD8^+$ T cells, as measured in the peripheral blood (Fig. 4*A*). Remarkably, the depletion of $CD8^+$ T cells had no effect on liver tumor burden (Fig. 4*B* and *C*) or distant metastasis (Fig. 4*D* and Supplementary Fig. 4*A*–*C*), suggesting these immune cells play a minimal role in controlling metastatic dissemination. Next, we used a genetic model of NK cell depletion, whereby the pro-survival gene *Mcl1* is conditionally deleted in NKp46-expressing cells ($Mcl1^{NKp46\Delta/\Delta}$)[14] resulting in a lack of NK cells (Fig. 4E). In contrast to $CD8^+$ T cell depletion, the absence of NK cells resulted in increased metastatic spread to the liver (Fig. 4*F* and *G*) and enhanced metastatic spread to lung (Fig. 4H) and kidney (Supplementary Fig. 4*D*–*F*). Notably, the rate of SQ primary tumor growth was unchanged in the absence of NK cells (Supplementary Fig. 4*G*), suggesting NK cells play a critical role in immunosurveillance of SCLC dissemination.

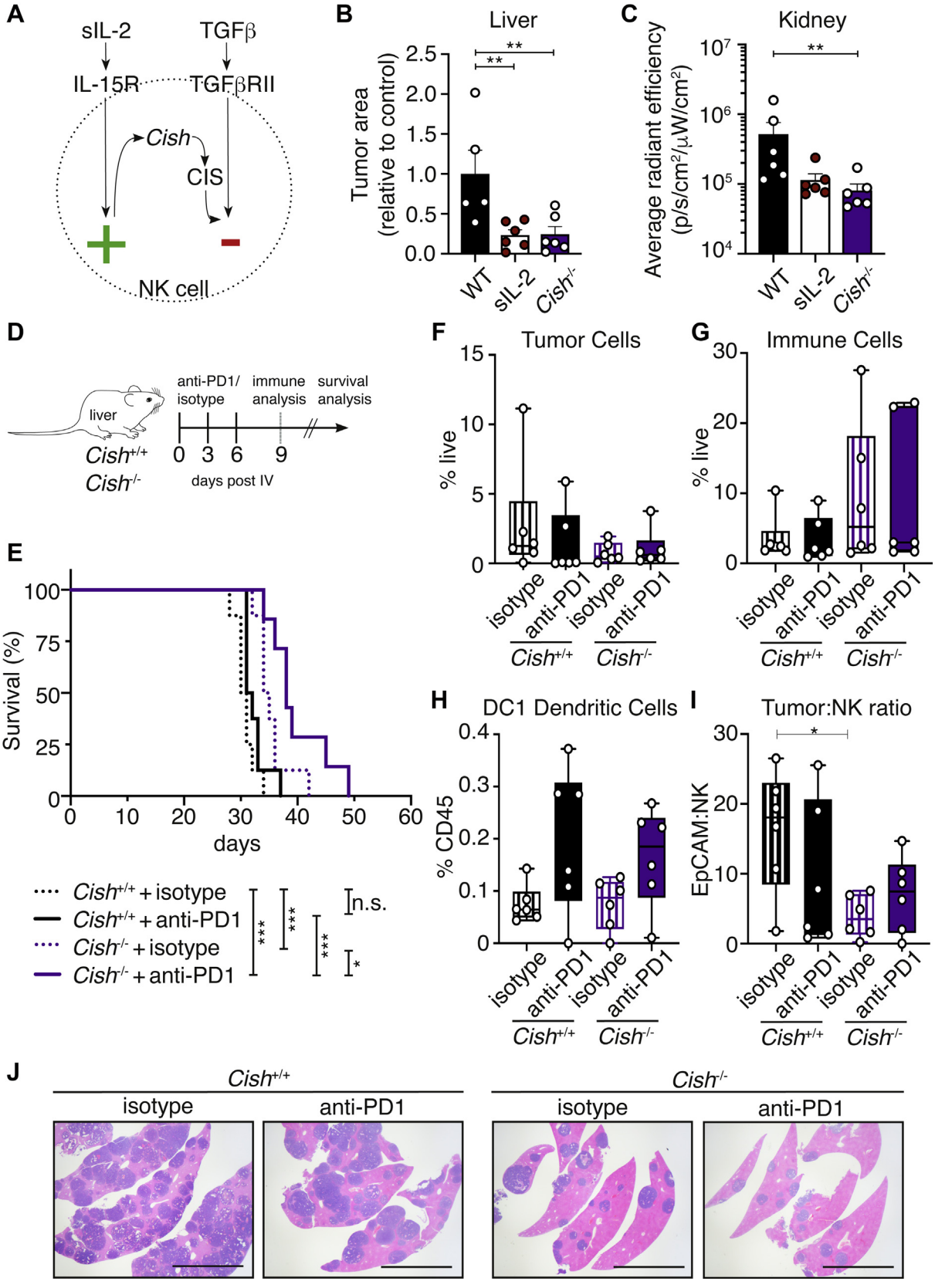

Figure 5. Activated NK cells are superior in the control of SCLC metastatic spread. (*A*) Schematic of NK cell activation pathways. Briefly, activation can be achieved through the delivery of sIL-2, which activates the IL-15R leading to NK cell activation. The gene *Cish*, transcribed into the protein CIS, is activated as a negative feedback mechanism to down-regulate

Given that the absence of NK cells resulted in an increase in metastatic burden, we set out to establish whether the activation of NK cells may be a viable therapeutic approach to control metastatic dissemination of SCLC. Although the activation and control of NK cells occurs through a vast number of mechanisms (reviewed in Souza-Fonseca-Guimaraes et al.[11]), we investigated three major pathways in the activation of NK cells (Fig. 5*A*). IL-15 is a critical mediator of NK cell biology and is up-regulated in inflamed tissue and cancers to prime NK cell activity. The suppressor of cytokine signaling protein CIS (encoded by *Cish*; cytokine-induced SH2 domain) is induced by IL-15 and was recently revealed to act as a potent intracellular NK checkpoint through negative feedback to IL-15 receptor signaling.[12] As a result, $Cish^{-/-}$ mice exhibit hyperactive NK cells enabling them to control tumor cell dissemination when challenged with metastatic melanoma and breast cancer transplantation models.[12] IL-15 signaling is modeled using sIL-2, a modified antibody and recombinant IL-2 complex (IL-2/S4B6 complex) that forces signaling through the IL-2Rβ/γ components of the IL-15 receptor complex in NK and $CD8^+$ T cells.[47] Initially, we modeled activation of NK cells through the IL-15 signaling pathway using either C57BL/6 mice injected with sIL-2 or $Cish^{-/-}$ recipient mice (Supplementary Fig. 5*A*–*D*). Strikingly, the metastatic burden of RP-T cells was markedly reduced in the livers of both sIL-2 and $Cish^{-/-}$ models (Fig. 5*B*) and at distant metastatic sites (Fig. 5*C* and Supplementary Fig. 5*E*–*G*). Together, these data confirm that NK cells with an uninhibited IL-15 pathway are superior in controlling the metastatic dissemination of SCLC tumor cells.

To confirm that the effects of IL-15 pathway activation were specific to NK cells themselves, we took an unambiguous genetic approach to NK cell activation. TGF-β is a direct inhibitor of IL-15–induced activation of the mTOR in NK cells (Fig. 5*A*), resulting in a metabolic blockade and a loss of antitumor effector function.[13] To remove the inhibitory "brake" function of TGF-β specifically in NK cells, we deleted TGF-β receptor II (TGFβRII) only in NKp46–expressing cells ($TGF\beta RII^{NKp46\Delta/\Delta}$).[19] Strikingly, SCLC metastatic burden was markedly depleted in the livers of $TGF\beta RII^{NKp46\Delta/\Delta}$ recipient mice (Supplementary Fig. 5*H* and *I*), as was metastasis to additional organs, such as the kidney (Supplementary Fig. 5*J* and *K*). Together, these data provide overwhelming evidence that NK cells are mediators of SCLC immunosurveillance, and their enhanced activity results in superior metastatic control.

Immunotherapy Provides Combined Benefit to SCLC Metastatic Dissemination

Having identified a critical role of NK cells in SCLC metastatic surveillance, we next investigated whether immunotherapy could enhance this effect. Recent evidence in metastatic melanoma models revealed a synergistic benefit of $Cish^{-/-}$ with ICB.[12] Therefore, we reasoned that there could be additional benefit of NK cell activation in trials such as the IMpower133.[10] To establish a synergistic response of combined NK and T cell immunotherapy in metastatic SCLC, we IV injected RP-NT cells into $Cish^{-/-}$ or $Cish^{+/+}$ recipient mice. After one cycle (days 0, 3, and 6) of anti–PD-1 or isotype treatment, the cohorts of mice were collected for immune activation analysis (days 9 and 25) or monitored for survival analysis (Fig. 5*D*). Critically, we identified that, in addition to enhanced $CD8^+$ T cell activation, NK cells were activated in response to anti–PD-1 treatment in the peripheral blood (Supplementary Fig. 6*A*–*D*). Moreover, anti–PD-1–treated $Cish^{-/-}$ mice displayed substantially greater tumor control compared with $Cish^{+/+}$ isotype-treated controls (30.5–38 d; $p = 0.0002$)

the activity of NK cells. The ligand TGFβ binds its receptor (TGFβRII) leading to reduced functionality of NK cells. (*B*) Quantification of liver metastatic burden 30 days after IV injection of RP-T cells into C57BL/6 controls (n = 6), C57BL/6 treated with sIL-2 (n = 6) and $Cish^{-/-}$ (n = 6) recipient mice. (*C*) Quantification of mCherry signal in distant metastases to the kidney in C57BL/6 control (n = 6), sIL-2 treated C57BL/6 (n = 6), and $Cish^{-/-}$ (n = 6) recipient mice. Mean ± SEM. Kruskal-Wallis test/Dunn's multiple comparisons test $^{**}p = 0.0045$. (*D*) Schematic of anti-PD-1 treatment study. Briefly, 0.5×10^6 RP-NT cells were injected IV into $Cish^{+/+}$ or $Cish^{-/-}$ mice (day 0) and treated with one cycle anti-PD-1 or isotype treatment (day 0, 3, 6). Short-term analysis cohort mice were collected at day 9, and survival analysis mice were collected when moribund and tumor burden was measured by liver histology. (*E*) Survival analysis of $Cish^{+/+}$ treated with isotype (n = 8), $Cish^{+/+}$ treated with anti-PD-1 (n = 8), $Cish^{-/-}$ treated with isotype (n = 8) and $Cish^{-/-}$ treated with anti-PD-1 (n = 7). Mantel-Cox test $Cish^{-/-}$ isotype versus anti-PD-1, $^{*}p = 0.0416$; $Cish^{+/+}$ versus $Cish^{-/-}$ treated with isotype control, $^{***}p = 0.0008$; $Cish^{+/+}$ versus $Cish^{-/-}$ treated with anti-PD-1, $^{***}p = 0.0008$. $Cish^{+/+}$ treated with isotype control versus $Cish^{-/-}$ treated with anti-PD-1, $^{***}p = 0.0002$. Flow cytometry analysis of tumor-bearing livers collected 25 days after IV injection of RP-NT cells and anti-PD-1 treatment (n = 6 mice/genotype/treatment arm) of (*F*) tumor cells ($EpCAM^+NCAM^+$); (*G*) immune cells ($CD45^+$); (*H*) DC1 dendritic cells ($CD11b^-CD103^+$), and (*I*) the ratio of tumor cells to NK cells. One-way ANOVA/Tukey's multiple comparisons test $Cish^{+/+}$ versus $Cish^{-/-}$ isotype-treated $^{*}p = 0.0461$. *(J)* Representative H&E-stained livers from cohort mice collected 25 days after IV injection of RP-NT cells and anti-PD-1 treatment. Scale, 5 mm. H&E, hematoxylin and eosin; IL-15R, interleukin-15 receptor; IV, intravenous; NK, natural killer; RP-NT, RP-nontransduced; RP-T, RP-transduced; n.s., not significant; PD-1, programmed cell death-protein 1; sIL-2, super IL-2; TGFβRII, TGFβ receptor II; TGFβ, transforming growth factor-β; WT, wild type.

(Fig. 5*E*). Next, we collected a cohort of mice 25 days after IV injection to analyze the tumor burden and immune infiltration in the liver. Strikingly, anti–PD-1–treated *Cish*$^{+/+}$ mice and all *Cish*$^{-/-}$ mice had a reduced proportion of tumor cells in the liver (Fig. 5*F*), which was accompanied by an increase in immune cells in *Cish*$^{-/-}$ mice (Fig. 5*G*). As an indicator of ICB activity, we identified increased abundance of DC1 dendritic cells in the livers of anti–PD-1–treated mice (Fig. 5*H*). Interestingly, NK cell infiltration into tumor-bearing livers was enhanced in *Cish*$^{-/-}$ mice, in which the number of NK cells was similar to the number of tumor cells (Fig. 5*I*), suggesting that in addition to enhanced NK cell activity (Supplementary Fig. 6*A*), *Cish*$^{-/-}$ NK cells are effective at targeting disseminated SCLC tumor cells. Consistent with these findings, histologically liver tumor burden was substantially controlled in *Cish*$^{-/-}$ recipient mice, with increased immunosurveillance detected after the addition of anti–PD-1 (Supplementary Fig. 6*E*). Taken together, our findings highlight the critical role of NK cell activation in SCLC metastatic dissemination and suggest that activated T and NK cells may synergistically act to exert an antitumor effect.

Discussion

In this study, we have reported that the heterogeneity of SCLC may be key to differential response to immunotherapy. Importantly, subsets characterized by *POU2F3*$^{+}$ and an immunoreactive fraction of *ASCL1*$^{+}$ SCLC displayed a marked increase in infiltration of NK and T cells in patient samples. Critically, the activation of NK cells is efficacious in the control of SCLC metastatic spread in a murine *Ascl1*$^{+}$ chemotherapy–naïve SCLC model.

Our bioinformatic studies revealed a significant correlation between NK score and the POU2F3^{+} subset of SCLC. Interestingly, a group of the ASCL1^{+} SCLC tumors exhibited a similar expression profile to that seen in POU2F3^{+} tumors, highlighting an unappreciated further level of heterogeneity within this subset of SCLC. POU2F3 is a marker of tuft cells, a chemosensory cell type that responds to external stimuli through the release of bioactive substances to regulate local epithelial and immune cell functions, akin to neuroendocrine cells.[48] Though their abundance in human lung tissue remains unclear,[49] single-cell RNA-seq studies performed on murine lung identified a distinct population of cells marked by differential expression of tuft cell genes, *Dclk1*, *Ascl2*, and *Foxn1*.[50,51] Although this subset represents approximately 16% of patients with SCLC,[3] it will be critical to patients with subtype SCLC who have responded to ICB therapies. While the bioinformatic causal link between SCLC subtypes and their immunogenicity does not directly address the response to immunotherapy, it is tantalizing to speculate that patients who exhibit increased immune infiltrate, such as POU2F3^{+} SCLC, display more durable responses. This could be addressed through generating sophisticated humanized mouse models and immune-competent murine SCLC models that mimic the heterogeneity of SCLC; as to date, there is no GEMM SCLC model described in the literature that represents POU2F3^{+} SCLC. In contrast, the RPM GEMM exhibits a low NK score, which we speculate would have a poor response to NK cell control; however, it was not included in our study. Together, these models would provide powerful tools to uncover potential differing immune-evasive mechanisms employed by SCLC cells, which will guide the development of alternative therapeutic approaches to treat this recalcitrant disease.

Although classical ICB approaches harness the activity of the adaptive immune system to elicit an antitumor response, the "next wave" of immunotherapeutic approaches is focused on exploiting facets of the innate immune system, of which NK cells are emerging as an attractive target (reviewed in Demaria et al.[52]). This is likely to be pertinent in tumors that have down-regulated HLA expression. Indeed, we recently reported that neuroendocrine tumors, including SCLC, exhibit transcriptional silencing of the HLA antigen processing pathway.[9] Our analyses also reveal differential expression levels of HLA and antigen presentation genes between SCLC subtypes. Although these findings may assist in explaining the success of ICB in only a minority of patients with SCLC,[10] paradoxically, it also strengthens the rationale on deploying NK cell activity to potentiate SCLC killing. Indeed, we reported that harnessing the cytotoxic capacity of NK cells through modulating IL-15 and TGF-β signaling was effective in restricting the dissemination of SCLC. There is growing evidence to support the efficacy of therapies that enhance tumor immunity through promoting cytotoxic function of NK cells. Small molecule inhibitors targeting TGFβR, such as galunisertib (LY2157299),[53] and neutralizing anti–TGF-β−1, -2, and -3 antibodies, have been reported to enhance NK cell activity in preclinical studies.[13,15] Interestingly, suppressing TGF-β activity within the tumor microenvironment and inhibiting the PD-1/PD-L1 pathway may provide a novel therapeutic approach to enhance antitumor response. This approach has led to the development of M7824 (MSB0011359C), a bifunctional fusion protein comprised of a monoclonal antibody targeting PD-L1 fused to the extracellular domain of human TGFβRII.[54] These approaches highlight an emerging area of interest to dampen such inhibitory signals.

There is emerging evidence that NK cells not only contribute direct antitumor function but also play an instrumental role in driving tumor inflammation through the recruitment of cDC1 and CD8^{+} T cells. In

mice and humans, responders to ICB have substantially higher infiltration of NK cells than nonresponders, and nonresponders can be induced to respond by targeting NK cell activity.[55,56] Thus, targeting both adaptive and innate cytotoxic cells will likely synergize to increase ICB response rates. The recent development of a humanized monoclonal antibody that blocks NKG2A, an inhibitory receptor expressed in the surface of both $CD8^+$ T and NK cells, exploits this cooperative nature of immune cell function.[57] Interestingly, anti-NKG2A (monalizumab) treatment of patients with advanced head and neck squamous cell carcinoma in combination with cetuximab is reporting promising results, with partial response observed in 31% of patients, an effect higher than expected from single agent alone. Studies exploring novel treatment approaches that augment the antitumor response of ICB are urgently required, particularly in SCLC. When combined with inhibition of the DNA damaged response pathway, for example, with PARP or CHK1 inhibitors, anti–PD-L1 treatment induced a durable antitumor response in preclinical models.[46] Thus, rational targeting of the tumor, tumor microenvironment, and multiple immune effectors should be investigated in combination cancer therapy trials.

Here, we find that SCLC metastasis is controlled by the cytotoxic activity of NK cells, and that their activation can provide superior control of tumor cell dissemination. Critically, SCLC subtypes express differential levels of immunoreactive transcripts, predicting infiltration of cytotoxic mediators into tumor tissue. Moving forward, application of T cell-mediated immunotherapy should be stratified by SCLC subtype and NK activating immunotherapy implemented in the SCLC setting.

Acknowledgments

This work was supported by an Australian National Health and Medical Research Council (NHMRC) project grant to Drs. Sutherland, Huntington, and Steinfort (1159955); to Dr. Souza-Fonseca-Guimaraes (1140406); a Priority-Driven Collaborative Cancer Research Scheme funded by Cure Cancer Australia with the assistance of Cancer Australia (1158085); and a generous charitable donation. Dr. Sutherland is supported by the Peter and Julie Alston Centenary Fellowship, Dr. Huntington is a NHMRC CDF2 Fellow (1124788), Dr. Steinfort holds an NHMRC Early Career Fellowship (1121880), Dr. Rautela holds a Victorian Cancer Agency Early Career Seed grant (ECSG18020), and Mr. Hess is supported by a University of Melbourne Research Scholarship. This work was made possible through the Victorian State Government Operational Infrastructure Support and Australian Government NHMRC IRIISS. The authors thank Kimmy Zhao and Leanne Taylor at the Victorian Cancer Biobank for collection, deidentification, and delivery of the patient material. The authors are grateful to L. Mackiewicz, K. Hughes, L. Scott, E. Loza, L. Spencer, and D. Boyd for animal husbandry; T. Camilleri and T. Kratina for genotyping; and S. Monard in the Walter and Eliza Hall Institute (WEHI) Flow Cytometry Facility and E. Tsui in the WEHI Histology Facility for support. The authors thank T. Oliver (Huntsman Cancer Institute) for reagents and protocols. The authors also thank S. Griffiths (Royal Melbourne Hospital), M. Pelligrini (WEHI), E. Vivier (Centre d'immunologie de Marseille-Luminy), and S. Karlsson (Lund University) for generously sharing mouse strains.

Supplementary Data

Note: To access the supplementary material accompanying this article, visit the online version of the *Journal of Thoracic Oncology* at www.jto.org and at https://doi.org/10.1016/j.jtho.2020.05.008.

References

1. National Cancer Institute. Surveillance, Epideriology, and End Results Program. 2020 SEER Cancer Statistics Review (CSR) 1975–2016. Accessed November 1, 2019 https://seer.cancer.gov/archive/csr/1975_2016/#contents.
2. van Meerbeeck JP, Fennell DA, De Ruysscher DK. Small-cell lung cancer. *Lancet*. 2011;378:1741–1755.
3. Rudin CM, Poirier JT, Byers LA, et al. Molecular subtypes of small cell lung cancer: a synthesis of human and mouse model data. *Nat Rev Cancer*. 2019;19:289–297.
4. Byers LA, Rudin CM. Small cell lung cancer: where do we go from here? *Cancer*. 2015;121:664–672.
5. Bunn PA Jr, Minna JD, Augustyn A, et al. Small cell lung cancer: can recent advances in biology and molecular biology be translated into improved outcomes? *J Thorac Oncol*. 2016;11:453–474.
6. Chen DS, Mellman I. Elements of cancer immunity and the cancer-immune set point. *Nature*. 2017;541:321–330.
7. Hellmann MD, Nathanson T, Rizvi H, et al. Genomic features of response to combination immunotherapy in patients with advanced non-small-cell lung cancer. *Cancer Cell*. 2018;33:843–852:e4.
8. Alexandrov LB, Nik-Zainal S, Wedge DC, et al. Signatures of mutational processes in human cancer. *Nature*. 2013;500:415–421.
9. Burr ML, Sparbier CE, Chan KL, et al. An evolutionarily conserved function of Polycomb silences the MHC class I antigen presentation pathway and enables immune evasion in cancer. *Cancer Cell*. 2019;36:385–401:e8.
10. Horn L, Mansfield AS, Szczęsna A, et al. First-line atezolizumab plus chemotherapy in extensive-stage small-cell lung cancer. *N Engl J Med*. 2018;379:2220–2229.
11. Souza-Fonseca-Guimaraes F, Cursons J, Huntington ND. The emergence of natural killer cells as a major target

in cancer immunotherapy. *Trends Immunol*. 2019;40:142–158.
12. Delconte RB, Kolesnik TB, Dagley LF, et al. CIS is a potent checkpoint in NK cell-mediated tumor immunity. *Nat Immunol*. 2016;17:816–824.
13. Viel S, Marçais A, Guimaraes FS, et al. TGF-beta inhibits the activation and functions of NK cells by repressing the mTOR pathway. *Sci Signal*. 2016;9:ra19.
14. Sathe P, Delconte RB, Souza-Fonseca-Guimaraes F, et al. Innate immunodeficiency following genetic ablation of Mcl1 in natural killer cells. *Nat Commun*. 2014;5:4539.
15. Rautela J, Dagley LF, de Oliveira CC, et al. Therapeutic blockade of activin-a improves NK cell function and antitumor immunity. *Sci Signal*. 2019;12:eaat7527.
16. Cursons J, Souza-Fonseca-Guimaraes F, Foroutan M, et al. A gene signature predicting natural killer cell infiltration and improved survival in melanoma patients. *Cancer Immunol Res*. 2019;7:1162–1174.
17. Mlecnik B, Bindea G, Angell HK, et al. Functional network pipeline reveals genetic determinants associated with in situ lymphocyte proliferation and survival of cancer patients. *Sci Transl Med*. 2014;6:228ra37.
18. Meuwissen R, Linn SC, Linnoila RI, Zevenhoven J, Mooi WJ, Berns A. Induction of small cell lung cancer by somatic inactivation of both Trp53 and Rb1 in a conditional mouse model. *Cancer Cell*. 2003;4:181–189.
19. Levéen P, Carlsen M, Makowska A, et al. TGF-beta type II receptor-deficient thymocytes develop normally but demonstrate increased $CD8^+$ proliferation in vivo. *Blood*. 2005;106:4234–4240.
20. Kägi D, Ledermann B, Burki K, et al. Cytotoxicity mediated by T cells and natural killer cells is greatly impaired in perforin-deficient mice. *Nature*. 1994;369:31–37.
21. Dalton DK, Pitts-Meek S, Keshav S, Figari IS, Bradley A, Stewart TA. Multiple defects of immune cell function in mice with disrupted interferon-gamma genes. *Science*. 1993;259:1739–1742.
22. DuPage M, Dooley AL, Jacks T. Conditional mouse lung cancer models using adenoviral or lentiviral delivery of Cre recombinase. *Nat Protoc*. 2009;4:1064–1072.
23. Xu Z, Sharp PP, Yao Y, et al. BET inhibition represses miR17-92 to drive BIM-initiated apoptosis of normal and transformed hematopoietic cells. *Leukemia*. 2016;30:1531–1541.
24. Best SA, Kersbergen A, Asselin-Labat ML, Sutherland KD. Combining cell type-restricted adenoviral targeting with immunostaining and flow cytometry to identify cells-of-origin of lung cancer. *Methods Mol Biol*. 2018;1725:15–29.
25. Hunter JD. Matplotlib: a 2D graphics environment. *Comput Sci Eng*. 2007;9:90–95.
26. Van Der Walt S, Colbert SC, Varoquaux G. The NumPy array: a structure for efficient numerical computation. *Comput Sci Eng*. 2011;13:22–30.
27. McKinney W. Data structures for statistical computing in python. Paper Presented at: Proceedings of the 9th Python in Science Conference. 2010;445:51–56; Austin, TX.
28. Pedregosa F, Varoquaux G, Gramfort A, et al. Scikit-learn: machine learning in Python. *J Mach Learn Res*. 2011;12:2825–2830.
29. Jones E, Oliphant T, Peterson P, et al. 2001 SciPy: Open Source Scientific Tools for Python. http://www.scipy.org/. Accessed July 1, 2019.
30. George J, Lim JS, Jang SJ, et al. Comprehensive genomic profiles of small cell lung cancer. *Nature*. 2015;524:47–53.
31. Mollaoglu G, Guthrie MR, Bohm S, et al. MYC drives progression of small cell lung cancer to a variant neuroendocrine subtype with vulnerability to aurora kinase inhibition. *Cancer Cell*. 2017;31:270–285.
32. Schaffer BE, Park KS, Yiu G, et al. Loss of p130 accelerates tumor development in a mouse model for human small-cell lung carcinoma. *Cancer Res*. 2010;70:3877–3883.
33. Gautier L, Cope L, Bolstad BM, Irizarry RA. Affy—analysis of Affymetrix GeneChip data at the probe level. *Bioinformatics*. 2004;20:307–315.
34. Huber W, Carey VJ, Gentleman R, et al. Orchestrating high-throughput genomic analysis with bioconductor. *Nat Methods*. 2015;12:115–121.
35. Team RC. *R: A Language and Environment for Statistical Computing*. Vienna, Austria: R Foundation for Statistical Computing; 2019.
36. Irizarry RA, Bolstad BM, Collin F, Cope LM, Hobbs B, Speed TP. Summaries of Affymetrix GeneChip probe level data. *Nucleic Acids Res*. 2003;31:e15.
37. mouse4302. db: Affymetrix Mouse Genome 430 2.0 Array annotation data (chip mouse4302). *R Package Version*. 2016;323.
38. Bult CJ, Blake JA, Smith CL, Kadin JA, Richardson JE, Mouse Genome Database Group. Mouse Genome Database (MGD) 2019. *Nucleic Acids Res*. 2019;47:D801–D806.
39. Foroutan M, Bhuva DD, Lyu R, Horan K, Cursons J, Davis MJ. Single sample scoring of molecular phenotypes. *BMC Bioinformatics*. 2018;19:404.
40. Newman AM, Liu CL, Green MR, et al. Robust enumeration of cell subsets from tissue expression profiles. *Nat Methods*. 2015;12:453–457.
41. Leong TL, Marini KD, Rossello FJ, et al. Genomic characterisation of small cell lung cancer patient-derived xenografts generated from endobronchial ultrasound-guided transbronchial needle aspiration specimens. *PLoS One*. 2014;9:e106862.
42. Steinfort DP, Siva S, Leong TL, et al. Systematic endobronchial ultrasound-guided mediastinal staging versus positron emission tomography for comprehensive mediastinal staging in NSCLC before radical radiotherapy of non-small cell lung cancer: a pilot study. *Medicine (Baltimore)*. 2016;95:e2488.
43. Mountain CF, Dresler CM. Regional lymph node classification for lung cancer staging. *Chest*. 1997;111:1718–1723.
44. Sutherland KD, Proost N, Brouns I, Adriaensen D, Song JY, Berns A. Cell of origin of small cell lung cancer: inactivation of Trp53 and Rb1 in distinct cell types of adult mouse lung. *Cancer Cell*. 2011;19:754–764.
45. Kwon MC, Proost N, Song JY, Sutherland KD, Zevenhoven J, Berns A. Paracrine signaling between tumor subclones of mouse SCLC: a critical role of ETS transcription factor Pea3 in facilitating metastasis. *Genes Dev*. 2015;29:1587–1592.

46. Sen T, Rodriguez BL, Chen L, et al. Targeting DNA damage response promotes antitumor immunity through STING-mediated T-cell activation in small cell lung cancer. *Cancer Discov*. 2019;9:646–661.
47. Spangler JB, Tomala J, Luca VC, et al. Antibodies to interleukin-2 elicit selective T cell subset potentiation through distinct conformational mechanisms. *Immunity*. 2015;42:815–825.
48. Yamashita J, Ohmoto M, Yamaguchi T, Matsumoto I, Hirota J. Skn-1a/Pou2f3 functions as a master regulator to generate Trpm5-expressing chemosensory cells in mice. *PLoS One*. 2017;12:e0189340.
49. Travaglini KJ, Nabhan AN, Penland L, et al. A molecular cell atlas of the human lung from single cell RNA sequencing. 2019. bioRxiv 742320.
50. Montoro DT, Haber AL, Biton M, et al. A revised airway epithelial hierarchy includes CFTR-expressing ionocytes. *Nature*. 2018;560:319–324.
51. Plasschaert LW, Zilionis R, Choo-Wing R, et al. A single-cell atlas of the airway epithelium reveals the CFTR-rich pulmonary ionocyte. *Nature*. 2018;560:377–381.
52. Demaria O, Cornen S, Daëron M, Morel Y, Medzhitov R, Vivier E. Harnessing innate immunity in cancer therapy. *Nature*. 2019;574:45–56.
53. Yingling JM, McMillen WT, Yan L, et al. Preclinical assessment of galunisertib (LY2157299 monohydrate), a first-in-class transforming growth factor-beta receptor type I inhibitor. *Oncotarget*. 2018;9:6659–6677.
54. Lan Y, Zhang D, Xu C, et al. Enhanced preclinical antitumor activity of M7824, a bifunctional fusion protein simultaneously targeting PD-L1 and TGF-β. *Sci Transl Med*. 2018;10:eaan5488.
55. Barry KC, Hsu J, Broz ML, et al. A natural killer-dendritic cell axis defines checkpoint therapy-responsive tumor microenvironments. *Nat Med*. 2018;24:1178–1191.
56. Zemek RM, De Jong E, Chin WL, et al. Sensitization to immune checkpoint blockade through activation of a STAT1/NK axis in the tumor microenvironment. *Sci Transl Med*. 2019;11:eaav7816.
57. André P, Denis C, Soulas C, et al. Anti-NKG2A mAb is a checkpoint inhibitor that promotes anti-tumor immunity by unleashing both T and NK cells. *Cell*. 2018;175:1731–1743.e13.